CrystEngComm

PAPER

View Article Online
View Journal | View Issue

Cite this: *CrystEngComm*, 2019, **21**, 5084

Construction of novel hybrid PdO–ZnO p–n heterojunction nanostructures as a high-response sensor for acetaldehyde gas†

Sanjit Manohar Majhi, * Hu-Jun Lee, Ha-Nui Choi, Ha-Young Cho, Jin-Soo Kim, Cheul-Ro Lee and Yeon-Tae Yu*

P–n heterojunction nanostructures (NSs) are emerging as a promising class of hybrid materials for gas-sensing applications. In this work, we report a facile, cost-effective synthesis technique to fabricate unique, hybrid PdO@ZnO p–n heterojunction NSs as high response and selective acetaldehyde gas sensors. Initially, Pd@ZnO core–shell NSs (CSNSs) were synthesized, and subsequently transformed into hybrid PdO@ZnO p–n heterojunction NSs by a simple high-temperature calcination method. The morphological study of the prepared hybrid NSs was carried out by transmission electron microscopy (TEM), which revealed that 10 ± 5 nm sized Pd nanoparticles (Pd NPs) were encapsulated in the center of the ZnO shell of 40–50 nm to form approximately 75–135 nm sized Pd@ZnO CSNSs. The more crystalline, flower-shaped PdO@ZnO p–n heterojunction NSs were formed after the Pd@ZnO CSNSs were calcined at 500 °C for 2 h. When employed as a gas sensor, the hybrid PdO@ZnO p–n heterojunction NSs demonstrated high sensitivity and selectivity to acetaldehyde gas amongst other gases (ethanol, CO, H_2, and CH_4). The PdO@ZnO p–n heterojunction NSs-based sensor delivered the highest response (R_a/R_g = 76) to 100 ppm acetaldehyde at 350 °C, as compared to the pristine ZnO NSs sensor (R_a/R_g = 18). The improved sensing performance of the hybrid PdO@ZnO p–n heterojunction NSs-based sensor over the pristine ZnO NSs-based sensor was attributed to the combination of the resulting synergistic effect due to the formation of the p–n heterojunction between PdO and ZnO NPs, the catalytic dissociation effect of PdO, and the high surface area of the PdO@ZnO p–n heterojunction NSs.

Received 9th May 2019,
Accepted 21st July 2019

DOI: 10.1039/c9ce00710e

rsc.li/crystengcomm

1. Introduction

The growing air pollution, due to various hazardous chemicals and volatile organic compounds (VOCs) that are released into the environment, poses a serious threat to human safety and health. Among different VOCs, acetaldehyde, a colorless, toxic, and flammable liquid with an irritating odor, which is found ubiquitously in indoor and outdoor environments, is regarded as one of the most common air pollutants. The common sources of acetaldehyde are cigarette smoke, wine, and household materials such as paints, chemical adhesives, resins, carpets, stains, rotten parts of wood furniture, waste food, and clothes. Due to its carcinogenic nature, long-time exposure to acetaldehyde causes serious health problems, such as imbalance in human metabolism and anti-oxidants and damage to the liver, DNA, and proteins.[1–6] Therefore, early monitoring of acetaldehyde around indoor and outdoor premises through efficient gas sensing systems is highly necessary to guarantee human safety. Hitherto, semiconductor-based metal oxides (MOs) have emerged as excellent candidates for gas-sensing materials, due to their innate advantageous attributes, such as low maintenance costs, simplicity in design, portability, and high sensing properties.[7] However, to meet further practical needs such as high response and selectivity, significant progress has been made in improving MOs gas sensing performance through different approaches such as functionalization of noble metal catalysts,[8–10] doping,[11] fabrication of p–n heterojunction nanostructures,[12–14] and UV illumination.[15,16]

For a few years, n-type MOs (n-MOs) have been more widely studied for gas sensing properties than p-type MOs (p-MOs), due to their high sensing characteristics. However, p–n heterojunction NSs-based gas sensors made from the combination of low sensitivity p-MOs with intrinsically highly sensitive n-MOs demonstrate enhanced sensing abilities.[13] Therefore, researchers have shown substantial interest in p–n heterojunction NSs, due to their enhanced gas-sensing

Division of Advanced Materials Engineering and Research Center for Advanced Materials Development, College of Engineering, Chonbuk National University, Jeonju, 561-756, South Korea. E-mail: yeontae@jbnu.ac.kr, sanjit.majhi@kaust.edu.sa; Fax: +82 63 270 2305; Tel: +82 63 270 2288

† Electronic supplementary information (ESI) available. See DOI: 10.1039/c9ce00710e

properties.[17] Recently, many researchers have started exploring the design of p–n heterojunction NSs with different synthetic strategies for gas-sensing applications. Lee *et al.* synthesized Co_3O_4-decorated ZnO nanowire (Co_3O_4–ZnO NW) structures by a high-temperature thermal evaporation method for ethanol and NO_2 gas sensing.[14] Recently, Zhang *et al.* synthesized p-type, Co_3O_4-octahedra NP decorated n-type TiO_2 nanofiber (Co_3O_4/TiO_2) heterostructures by an electro spinning method, followed by a hydrothermal technique, and studied the heterostructures for CO gas sensing.[18] Baik *et al.* proposed air-bridged NW junction arrays of n-ZnO/p-CuO for H_2S gas-sensing applications, which were prepared by e-beam evaporation followed by chemical vapor deposition (CVD) methods.[19] Recently, Lee *et al.* proposed the formation of CuO–TiO_2 p–n heterojunction CSNWs by a simultaneous process of lithography and high-temperature heat treatment method, followed by an atomic layer deposition (ALD) method for the investigation of NO_2 and CO gas-sensing properties.[20] Nonetheless, most of these p–n junction-based sensing materials are associated with complex synthesis procedures or the use of special instruments. In addition, the random distribution or loading of oxides onto the surface might result in lower accessibility due to the complete or partial blockage of active sites for gas adsorption. Additionally, a lack of well-formed p–n junctions due to the non-uniform deposition of oxide catalysts may result in low sensing performance.[21] In this context, synthesizing p–n heterojunction NSs with a facile and novel approach for high gas-sensing performance would provide a great advantage.

Recently, the design and application of CSNSs, where noble metal or MO cores are coated with another MO shell, have gained substantial interest, due to the fascinating properties offered by the composite NSs. The increased surface area, high chemical and thermal stability, improved interface between the two individual components, and good protection of core materials from harsh conditions and aggregation are special attributes of CSNSs that demonstrate their potential in gas-sensing applications.[22] Ever since our group's pioneering contributions towards CSNS gas sensors,[23] tremendous efforts have been devoted to the synthesis of CSNSs to improve their sensing performance.[24–27] However, all of these reported materials were based on noble metal- MO-based CSNSs, and only a few reports of p–n heterojunction gas sensors based on CSNSs have been made.

Amongst the different n-MO-based gas sensors, zinc oxide (ZnO) with a band gap of 3.36 eV stands out as a promising sensing material due to its good chemical and high thermal properties, high electron mobility (~200 $cm^2\ V^{-1}\ S^{-1}$),[28] ease of synthesis with controlled morphology, low cost, and environmental friendliness. Although ZnO-based CSNSs have been reported for sensing applications, most of them are metal@ZnO (M@n-MO) CSNSs, which are Schottky junction type gas-sensing materials. In such M@n-MO CSNS-based gas sensors, the most frequently chosen core material was gold (Au) NPs. Palladium (Pd) noble metal is a well-known catalyst that is used for electronic sensitization and spillover effects in gas-sensing applications.[29] However, Pd metal is often prone to oxidation during high-temperature treatments, forming PdO which is a p-type MO.[30] Recent studies have utilized Pd and PdO NPs for many VOC sensing applications.[31] Hence, it would be interesting to study the gas sensing properties of the combination of PdO and ZnO, in order to design a p–n heterojunction NSs in a novel way. Therefore, the current study's novelty is the design of p–n heterojunction NSs using a p-MO (PdO) as the core and an n-MO (ZnO) as the shell, synthesized by a facile wet chemical method, and their integration into a high-performance gas-sensing device. We first synthesized Pd@ZnO CSNSs with a facile, low-temperature synthesis technique. Then, PdO@ZnO p–n heterojunction NSs were prepared by an *in situ* calcination method at high temperature, and employed for gas-sensing performance measurements. The PdO NPs were encapsulated inside the ZnO shell, and formed a well-defined CS type morphology with an intimate contact with the ZnO shell. To the best of our knowledge, research on the fabrication of PdO@ZnO p–n heterojunction NSs and their gas-sensing performance has never been reported previously. In this work, we investigate the details of the synthesis procedure, structural properties, surface morphology, and oxidation behavior of the Pd core at different calcination temperatures. When utilized as a potential gas sensor, our designed hybrid PdO@ZnO p–n heterojunction NSs show high sensing capabilities towards acetaldehyde, compared to different analytes. We discuss the effects of p–n heterojunction formation on the acetaldehyde gas sensing properties and their mechanisms.

2. Experimental section

2.1 Chemicals and materials

L-Ascorbic acid (AA; 99.5%) and hydrochloric acid (HCl) were purchased from Showa Chemicals Co. Ltd., Japan. Palladium(II) chloride ($PdCl_2$, 99%), hexamethylenetetramine (HMTA, 99%), hexadecyltrimethylammonium bromide (CTAB; 99%), and zinc nitrate hexahydrate ($Zn(NO_3)_2{\cdot}6H_2O$, 98.0%) were purchased from Sigma-Aldrich. All of the above chemicals used in this work were of analytical grade, and were used as received.

2.2 Synthesis procedures of Pd NPs and PdO@ZnO CSNSs

Prior to the synthesis of Pd NPs, 10 mM H_2PdCl_4 solution was firstly prepared from the reaction of $PdCl_2$ and HCl. For the Pd NP synthesis, 10 mM H_2PdCl_4 (2.5 mL) was mixed with 12.5 mM CTAB solution (50 mL), followed by heating with stirring. When the reaction temperature reached 99 °C, 0.4 mL of fresh AA was immediately dropped into the above solution, and further stirring was continued for up to 5–10 min. A change of color from orange to brownish in the obtained Pd NPs was noticed. The prepared Pd NPs were used for further preparation of the Pd@ZnO CSNSs. To synthesize the Pd@ZnO CSNSs, calculated amounts of CTAB (0.1465 g), AA (0.0354 g), $Zn(NO_3)_2{\cdot}6H_2O$ (0.120 g), and HMTA

(0.0564 g) were added one-by-one to a vial with 100 mL volume capacity, which had 50 mL of distilled (DI) water under suitable stirring. The molar ratios of Zn^{2+}/CTAB and Zn/HMTA were fixed at 1, while the molar ratio of AA/Zn^{2+} was fixed at 0.5. Finally, 3.2 mL of the prepared Pd NPs were added to the above solution with further stirring up to 5–10 min. The vial containing the final solution was sealed and heated inside an oven at 86 °C for 8 h. The Pd@ZnO CSNSs obtained were centrifuged to remove unreacted ions, followed by washing with DI water. Similarly, the pristine ZnO NSs were synthesized by following the above method without Pd NPs. The PdO@ZnO CSNSs were obtained directly by calcining the as-synthesized pristine Pd@ZnO CSNSs at 500 °C for 2 h, which were further examined by X-ray diffraction (XRD) and electron microscopy analysis. The as-synthesized pristine ZnO NSs were also calcined at 500 °C for 2 h for further characterization. Fig. 1 shows a schematic of the synthesis procedures for Pd NPs, ZnO NSs, and PdO@ZnO CSNSs.

2.3 Sample characterization

Morphological analysis of the as-prepared samples of ZnO NSs and PdO@ZnO CSNSs was carried out by TEM (Hitachi-H7650). Selected area diffraction (SAED), high-resolution TEM (HR-TEM), and high-resolution real-time line scan analysis were performed using a Zeiss EM-912, Omega. The XRD patterns of the prepared samples were analyzed by X-ray diffractometry (D/Max-2005, Rigaku) with a Cu-K_α, target (λ = 1.54178 Å). A Micrometrics instrument (TriStar 3000) was used to measure the Brunauer–Emmett–Teller (BET) nitrogen adsorption–desorption isotherms.

2.4 Preparation of sensor devices and gas sensing measurements

To fabricate the sensor devices of pristine ZnO NSs and PdO@ZnO p–n heterojunction NSs, a paste was prepared from the fine mixture of both samples (10 mg) and α-terpineol. The prepared paste was screen-printed using a glass slide onto the Pt-electrode-based interdigital alumina board (electrode area: 10 mm × 10 mm) with subsequent drying at 60 °C. The Pt-electrode-based interdigital alumina board was purchased from Ogam Technology Co. Ltd., South Korea. The prepared sensor devices were then heat-treated at 500 °C for 2 h in air prior to the gas-sensing measurement. Fig. S1 of the ESI† shows a schematic of the current sensor device preparation procedure. The prepared sensors were tested at various temperatures (150–400 °C), in the presence of different test gases. The maximum flow of gases in the mass flow controller (MFC) was 100 sccm. Nitrogen (background gas) and dry air (21% oxygen) were used during the gas-sensing test. A resistance meter (Agilent 34970A) was

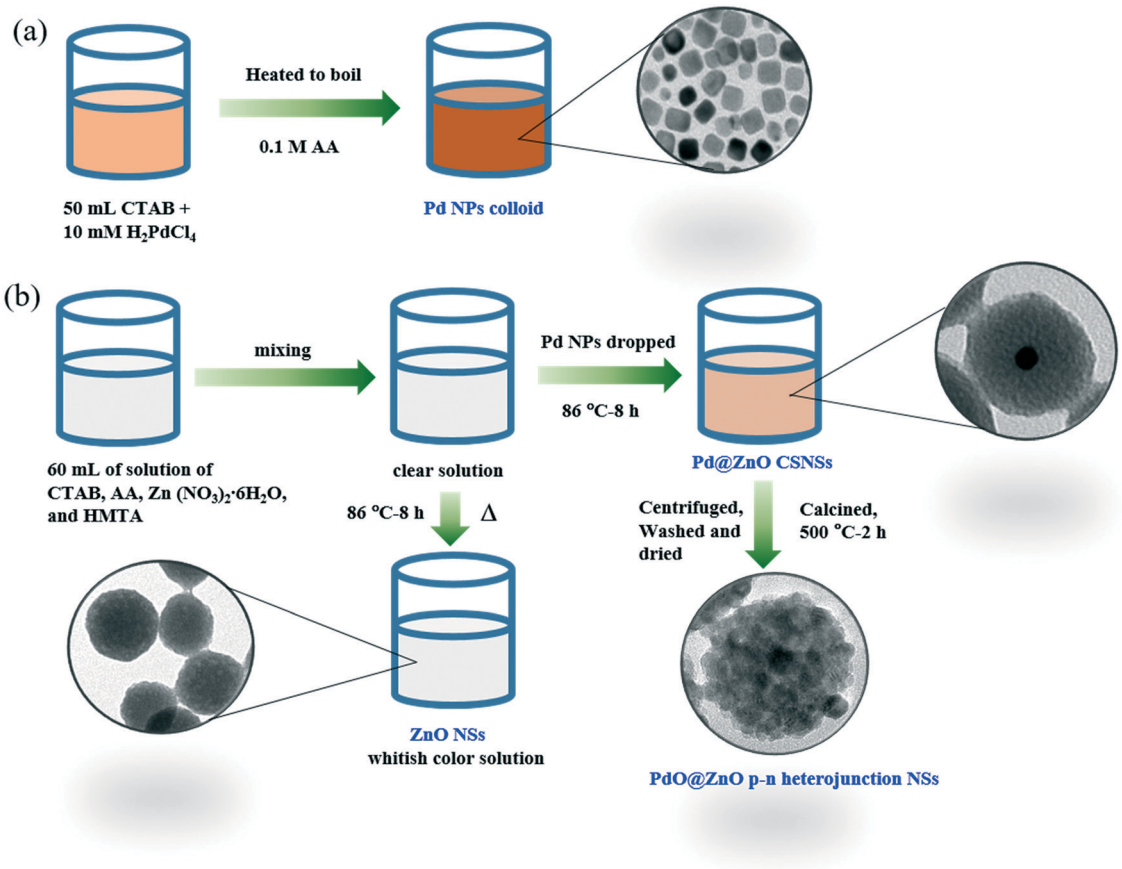

Fig. 1 Schematics of the synthesis processes of (a) Pd NPs, (b) ZnO NSs and PdO@ZnO CSNSs.

used to observe the resistance changes of the sensor devices before and after the supply of target gases, where R_a and R_g were the resistance measured in air and target gas, respectively. Fig. 2 shows a schematic of the homemade gas-sensing set-up that was used for our sensing experiments.

3. Results and discussion

3.1 Synthesis and characterization of the pristine ZnO NSs and Pd@ZnO CSNSs

Scheme 1 illustrates the facile, two-step synthesis process of the Pd@ZnO CSNSs by a low- temperature hydrothermal method. The synthesized Pd@ZnO CSNSs were further used to prepare PdO@ZnO p–n heterojunction NSs for the investigation of gas sensing properties. The possible growth process of the ZnO shell around the CTAB stabilized Pd NPs is as follows (as presented schematically in Scheme 1). First, AA and Zn^{2+} started to form an AA–Zn^{2+} complex due to the polyhydroxy acid nature of AA. Then, the concentration of OH^- ions in the solution increased due to the addition of HMTA, and they eventually attached to the AA–Zn^{2+} complex to form the $[AA–Zn(OH)_4]^{2-}$ complex. Meanwhile, the addition of CTAB stabilized the Pd NPs which results in the $[CTAB–AA–Zn(OH)_4]^{2-}$ complex being formed when $[AA–Zn(OH)_4]^{2-}$ reacted with the CTAB molecules on the Pd NP surface. This electrostatic attraction between the $[AA–Zn(OH)_4]^{2-}$ complex and the CTAB molecules went on further and eventually formed net-like chains centered around Pd NPs.[32,33] CTAB and AA behaved as templates, helped to stabilize the core and shell materials, and also helped to obstruct the continual growth of the ZnO shell. Finally, a dense ZnO shell around the Pd NPs was formed after the mixture solution was heated and aged for a long time, due to hydroxyl condensation reactions.[32]

The morphology and structural characterization of the prepared pristine ZnO NSs and Pd@ZnO CSNSs was carried out in detail by TEM, STEM, SAED, and HR-TEM observations. The TEM image in Fig. 3(a) shows that Pd NPs of mostly cubic shapes along with a few spherical shapes were formed with sizes ranging from 5 to 15 nm. Fig. 3(b) and (c) display the typical TEM images of Pd@ZnO CSNSs with nearly spherical shapes that were synthesized at 86 °C, where the Pd core and ZnO shell can be easily distinguished. The Pd@ZnO CSNSs had an average diameter of 80–120 nm, and 10–15 nm sized Pd NPs were centered in a 40–45 nm thick ZnO shell. On the other hand, the pristine ZnO NSs had an average diameter of 75–135 nm, which were formed without the use of Pd NPs (Fig. 3(d)). It is apparent from the TEM analysis of both the pristine ZnO NSs and Pd@ZnO CSNSs that the surfaces of the ZnO shell do not exhibit any crystalline primary particles, which is mainly due to the presence of CTAB ions on ZnO surfaces.[32] To further study the oxidation of palladium and the crystallinity of ZnO, the synthesized samples of both Pd@ZnO CSNSs and ZnO NSs were calcined at 500 °C for 2 h.

Fig. 4(a) and (b) show the TEM and STEM images of the calcined pristine ZnO NSs and Pd@ZnO CSNSs. It is notable that both the Pd@ZnO CSNSs and the pristine ZnO NSs which were obtained after being calcined at 500 °C were crystalline in nature without much difference in their surface morphology, in terms of their shapes and sizes. The smooth surface of the ZnO shell was distorted to a crystalline surface, with many aggregated primary particles (~10–20 nm). Fig. S2 of the ESI† shows a high-resolution TEM-EDS line-scan mapping, which was analyzed to determine the element content and distribution of the prepared material of PdO@ZnO p–n heterojunction NSs. It is clear that all the elements, such as Pd, Zn, and O, were present throughout the spectrum of the

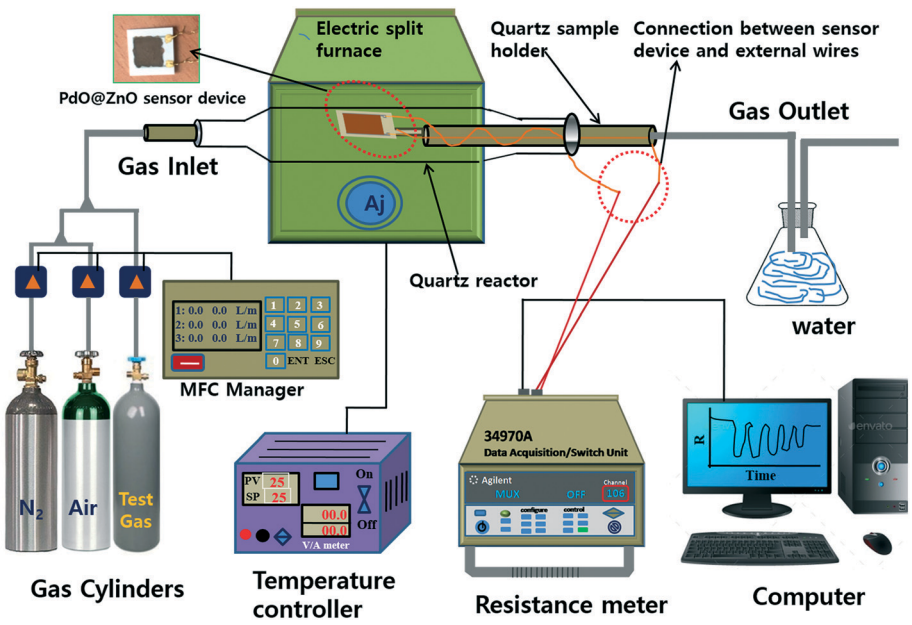

Fig. 2 Schematic of the laboratory gas-sensing measurement set-up.

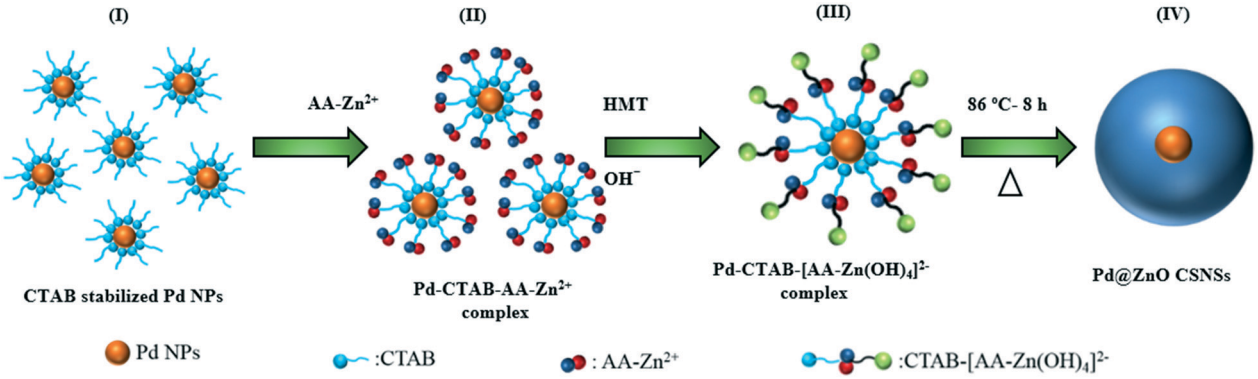

Scheme 1 Schematic of the possible formation of Pd@ZnO CSNSs.

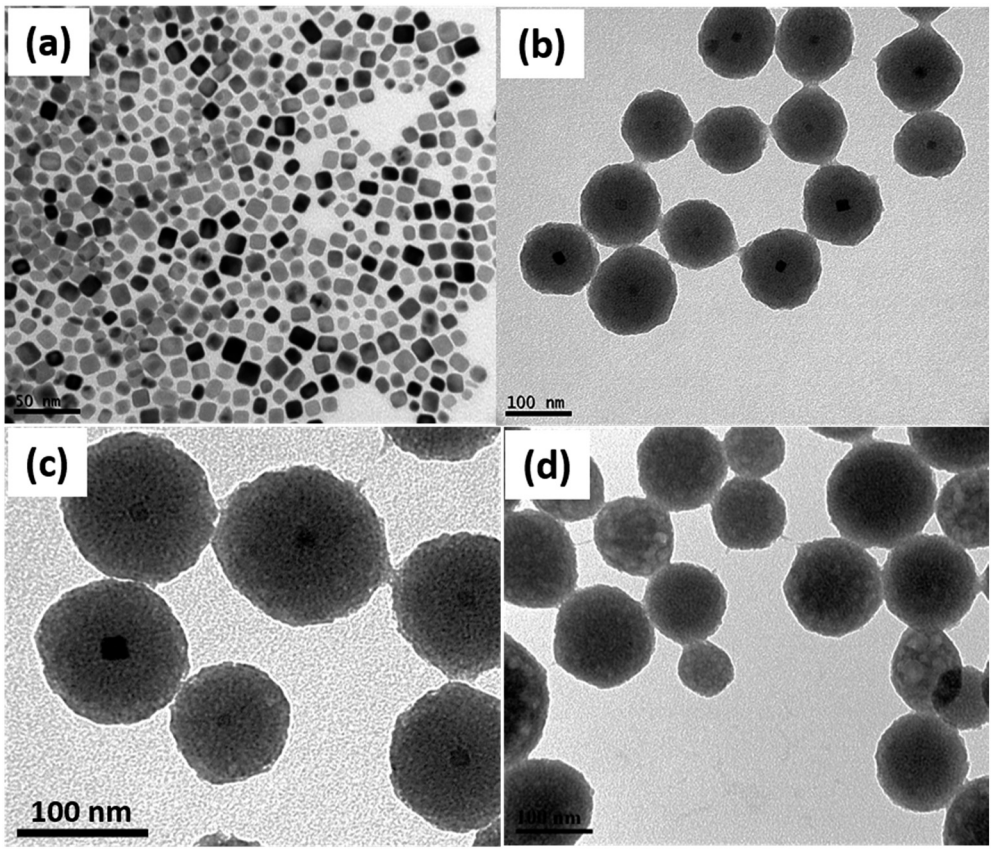

Fig. 3 TEM images of (a) Pd NPs, (b) and (c) as-synthesized Pd@ZnO CSNSs, and (d) pristine ZnO NSs.

PdO@ZnO p–n heterojunction NSs. Fig. S3 of the ESI† shows a few TEM images and the corresponding HAADF images of the PdO@ZnO p–n heterojunction NSs with HR-TEM. Since the Pd NPs were more or less of the same size as the ZnO NPs, it appears that the core NPs were mixed with ZnO NPs. However, the HAADF-STEM images (Fig. S3(b)–(d), (f), (k), and (l) of the ESI†) show that the core was clearly distinguishable. Fig. 4d shows the high-magnification HRTEM image of single Pd@ZnO CSNSs from the white rectangular mark in Fig. 4c, which illustrates the interface of Pd and ZnO. This demonstrates that the Pd core was changed to PdO, and the lattice spacing of 0.26 and 0.24 nm corresponds to the (101) plane of PdO and ZnO. It is thus confirmed that, at a calcination temperature of 500 °C, the Pd metal core of Pd@ZnO CSNSs was oxidized to PdO.

Hence, to further observe the oxidation behavior, the prepared Pd@ZnO CSNS material was calcined at various temperatures ranging from 100–500 °C, and an XRD analysis was then carried out, which is shown in Fig. 5. It can be seen that the Pd core started to oxidize from 300 °C, because in the 300 °C profile, the XRD peak of Pd has almost disappeared due to oxidation. On the other hand, the crystallinity of ZnO

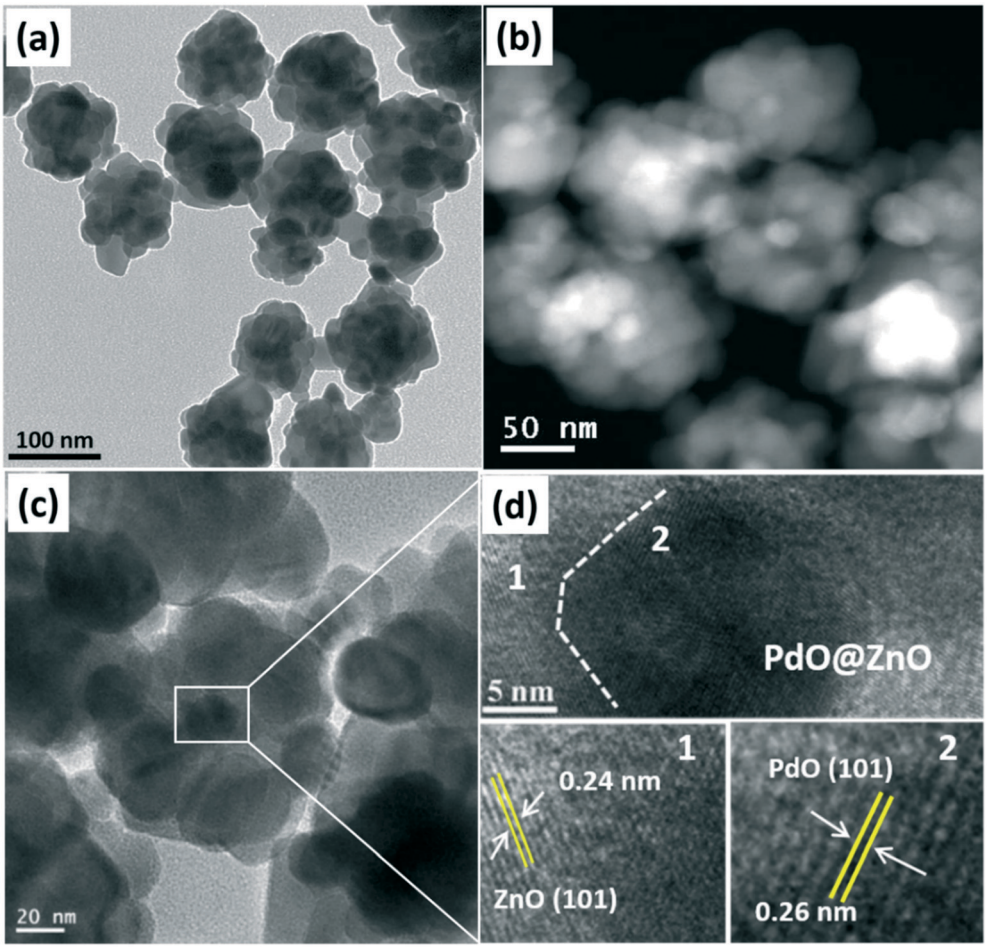

Fig. 4 (a) TEM images of pristine ZnO NSs calcined at 500 °C, (b) HAADF-STEM image of PdO@ZnO p–n heterojunction NSs, (c) single PdO@ZnO p–n heterojunction NSs calcined at 500 °C, and (d) the corresponding HRTEM image showing the PdO and ZnO interface with lattice fringes obtained from (c).

was greatly increased in the 400 °C calcination temperature profile. When the temperature was increased to 500 °C, complete oxidation of Pd to PdO could be observed. Therefore, the Pd@ZnO CSNS sensing material, which was calcined at 500 °C for 2 h, will henceforth be designated simply as PdO@ZnO p–n heterojunction NSs, and this sample's gas-sensing properties were further investigated, along with the pristine ZnO NSs. Fig. 6 illustrates the nitrogen adsorption–desorption isotherms of the pristine ZnO NSs and PdO@ZnO p–n heterojunction NSs. Fig. 6 shows that of all the isotherms agreed well with a type IV isotherm.[34] The specific BET surface area of the pristine ZnO NSs and PdO@ZnO p–n heterojunction NSs was measured and found to be 15.27 and 24.01 $m^2 g^{-1}$, respectively.

3.2 Gas sensing performance of the pristine ZnO NSs and PdO@ZnO p–n heterojunction NSs

The gas-sensing properties of the pristine ZnO NSs and PdO@ZnO p–n heterojunction NSs sensors were investigated by testing their acetaldehyde gas responses at different operating temperatures (150 to 400 °C), in order to optimize the working temperature at which the maximum response is obtained, which is shown in Fig. 7. The appearance of a volcano-shaped graph that indicates an "increase-maximum-decrease" response behavior can be seen from Fig. 7(a), which is obvious in the case of MO-based gas sensors. This may be attributed to the temperature-dependent reaction between the chemisorbed oxygen ions and target gas molecules. As can be seen, below the optimum working temperature (350 °C), the target acetaldehyde gas molecules do not have sufficient thermal energy to react with oxygen species.[35,36] The response of the PdO@ZnO p–n heterojunction NSs sensor increased gradually from 150 to 350 °C, which could be due to the obtained thermal energy being high enough to overcome the activation energy barrier for the sensing reaction. However, a further increase of the operating temperature resulted in a decreased response for the PdO@ZnO p–n heterojunction NSs sensor, which may be due to the difficulty in adsorbing both oxygen and target gas molecules on the sensor surface at high temperatures.[35] The highest response obtained for the PdO@ZnO p–n heterojunction NSs sensor was 76. The pristine ZnO NSs sensor also demonstrated a similar kind of increase–decrease sensing behavior (Fig. 7(a)).

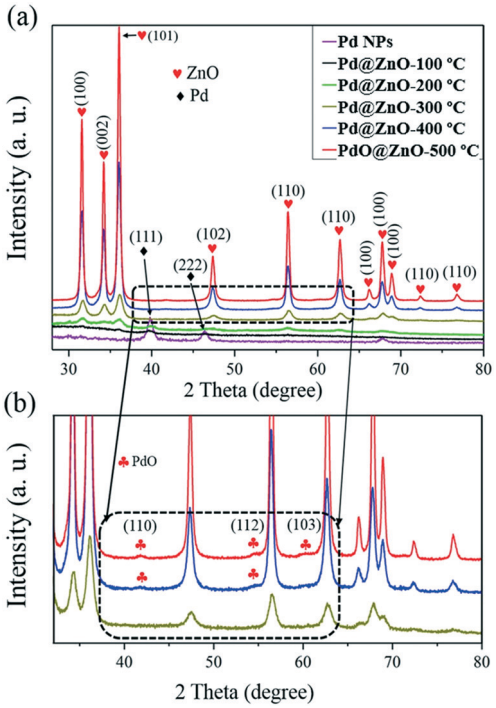

Fig. 5 (a) XRD profiles of the Pd NPs (as-synthesized) and Pd@ZnO CSNSs (calcined at different temperatures), and (b) magnified version of the XRD profiles of Pd@ZnO CSNSs (calcined from 100–300 °C) and PdO@ZnO p–n heterojunction NSs (calcined at 400–500 °C).

For the pristine ZnO NSs sensor, the maximum response (R_s = 22) was obtained at 375 °C operating temperature. The acetaldehyde response for the PdO@ZnO p–n heterojunction NSs-based sensor was higher than that for the pristine ZnO NSs sensor at each temperature. Thus, the PdO@ZnO p–n heterojunction NSs sensor demonstrated improved response at low working temperature. Fig. 7(b) displays the response transient of the pristine ZnO NSs and PdO@ZnO p–n heterojunction NSs sensors for acetaldehyde gas-testing in a descending order, with various concentrations of 2–100 ppm at 350 °C. Fig. 7(b) shows that both sensors demonstrated n-type sensing characteristics, that is, the resistance increases in air and then decreases after the introduction of acetaldehyde gas. The response of the pristine ZnO NSs sensor at 350 °C was found to be 18. The baseline resistance in air (R_a) of the PdO@ZnO p–n heterojunction NSs sensor was higher than that of the pristine ZnO NP sensor. The response and recovery times of the PdO@ZnO p–n heterojunction NSs and pristine ZnO NSs sensors were measured, and are shown in Fig. S4 of the ESI.† The response time (T_{resp}) of the PdO@ZnO p–n heterojunction NSs was found to be 108 s, which is faster than that of the pristine ZnO NSs (138 s). On the other hand, the recovery times (T_{recv}) of the PdO@ZnO p–n heterojunction NSs and pristine ZnO NSs were found to be 540 and 388 s, respectively. Fig. 7(c) illustrates the concentration-dependent response behavior of both sensors, which indicates that as the concentration of acetaldehyde is increased from 2 to 100 ppm, the response increases. The maximum response of the PdO@ZnO p–n heterojunction NSs sensor for 100 ppm acetaldehyde was found to be 76, whereas at 2 ppm the response value was 1.12. The sensitivity and selectivity are the two most crucial parameters for any gas sensor. Therefore, both sensors were tested for different analytes at 350 °C to obtain the highest response which is illustrated in Fig. 7(d). Among all the gases, the PdO@ZnO p–n heterojunction NSs sensor demonstrates the most enhanced response and highest selectivity to acetaldehyde gas. In addition to the sensitivity and selectivity, reproducibility is also an important parameter for gas sensors. Therefore, both the pristine ZnO NSs and PdO@ZnO p–n heterojunction NSs sensors were tested for 100 ppm acetaldehyde at 350 °C, which is shown in Fig. S5 of the ESI.† It can be observed that the sensors demonstrate good repeatability with consistent responses, even after eight cycles of testing in air and acetaldehyde atmospheres. Fig. S6 of the ESI† presents the long-term stability of the sensors based on PdO@ZnO p–n heterojunction NSs and ZnO NSs tested at 350 °C for 100 ppm acetaldehyde. The testing was conducted for a period of two weeks. It was found that the responses of both sensors had relatively small fluctuations during the testing, which demonstrates the stable and reliable operation of acetaldehyde sensing. Furthermore, Table 1 summarizes the comparison of gas sensing performance between our PdO@ZnO p–n heterojunction NSs sensor and previously reported sensors. Table 1 shows that the PdO@ZnO p–n heterojunction NSs sensor demonstrates relatively good acetaldehyde sensing properties, in comparison to previous sensors.

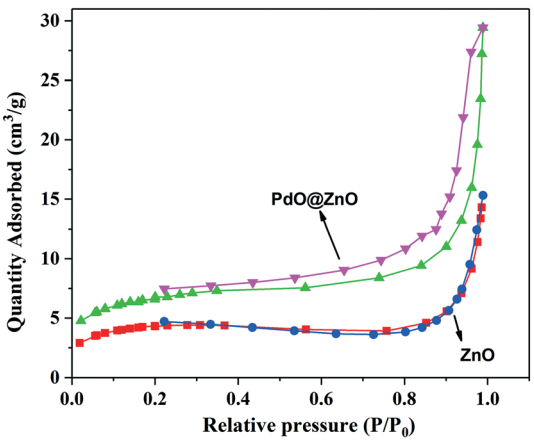

Fig. 6 Nitrogen adsorption–desorption isotherms of the pristine ZnO NSs and PdO@ZnO p–n heterojunction NSs.

4. Gas-sensing mechanism of the PdO@ZnO p–n heterojunction CSNS sensor

The sensing mechanism for the improved response of the PdO@ZnO p–n heterojunction NSs is explained here, based

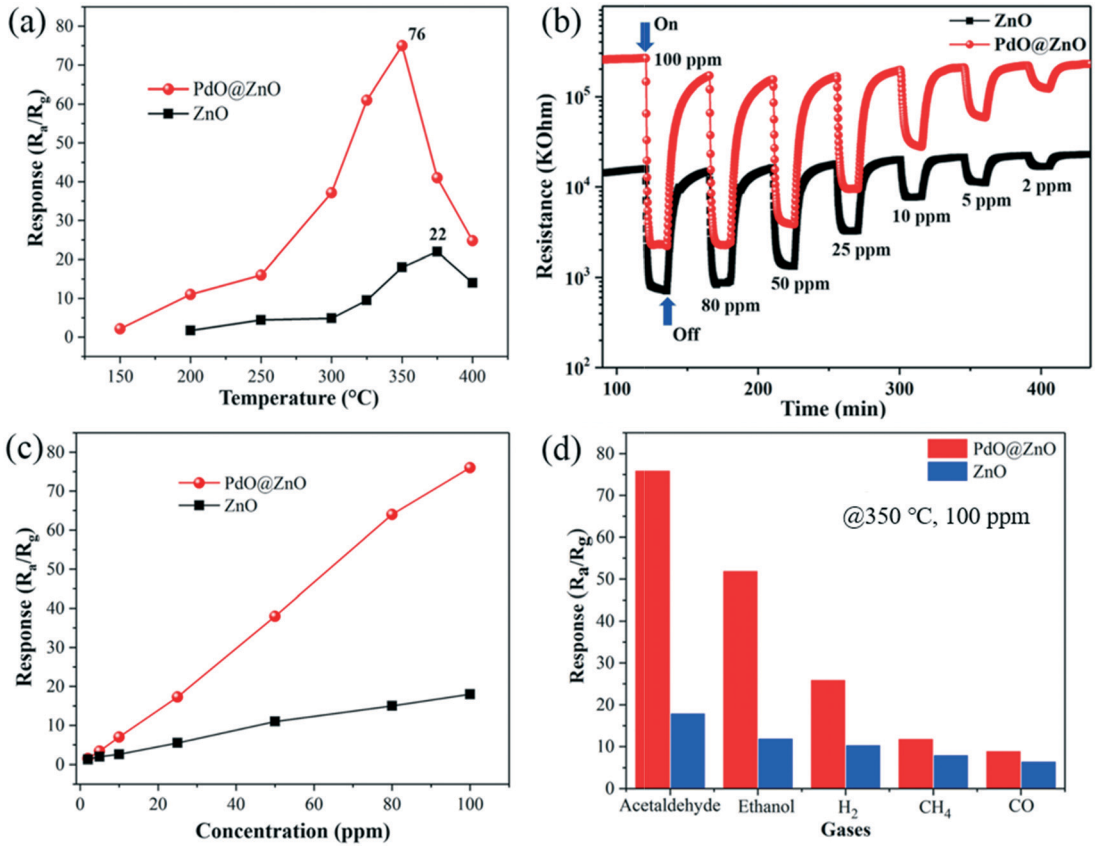

Fig. 7 (a) Responses of the pristine ZnO NSs and PdO@ZnO p–n heterojunction NSs-based sensors for 100 ppm acetaldehyde at different testing temperatures, (b) dynamic response transients of the pristine ZnO NSs and PdO@ZnO p–n heterojunction NSs for 100 ppm acetaldehyde at 350 °C, (c) variation of responses with respect to the variation of acetaldehyde concentration at 350 °C, and (d) summary of responses *versus* different analytes of the pristine ZnO NSs and PdO@ZnO p–n heterojunction NSs for 100 ppm acetaldehyde at 350 °C.

on the experimental findings. The gas-sensing mechanism of the pristine ZnO NSs sensor, which is a typical n-MO, has been extensively reported, based on the adsorption and desorption of oxygen and target gas molecules.[43,44] Initially, when the ZnO NSs sensor is exposed to air atmosphere, oxygen molecules are chemisorbed on the sensor surface and then capture conduction band electrons to generate ionized oxygen species such as O_2^-, O^- and O^{2-}, which results in an increase of the resistance of the ZnO NSs sensor due to the formation of electron depletion layers. However, in acetaldehyde environments, acetaldehyde reacts with these chemisorbed oxygen ions, and then releases the trapped electrons back to the ZnO NSs sensor. As a result, the width of the depletion layer decreases, and thus the resistance as well. The possible reactions are as follows:[39,40]

$$CH_3CHO_{(gas)} \leftrightarrow CH_3CHO_{(ads)} \quad (1)$$

$$CH_3CHO_{(ads)} + 50_{(ads)}^- \leftrightarrow 2CO_{2(gas)} + 2H_2O + 5e^- \quad (2)$$

On the other hand, the introduction of PdO in the core to obtain the PdO@ZnO p–n heterojunction NSs sensor significantly improved the sensing performance and its sensing mechanism is different from that of the pristine ZnO NSs sensor. The improved sensing performance of the PdO@ZnO p–n heterojunction NSs sensor compared to that of the pristine ZnO NSs sensor can be attributed to the electronic and chemical sensitization effects. PdO NPs play a significant role in the enhancement of sensing performance, and are involved in both of the above mechanisms.

In the electronic sensitization effect, a typical p–n heterojunction will be established between p-PdO and n-ZnO NPs for PdO@ZnO NSs. Since the work function of PdO (7.9 eV) is higher than the work function of ZnO (5.3 eV), the electrons in the ZnO conduction band will transfer to that of PdO, while the holes will transfer towards ZnO, until the Fermi level (E_f) of the system is equalized.[30,45] Thus, the PdO/ZnO p–n heterojunction will generate a wider depletion layer, and thus energy band bending at the interface of the PdO@ZnO p–n heterojunction NSs sensor (as shown in Fig. 8(a)). As a result, the resistance of the PdO@ZnO p–n heterojunction NSs sensor increases significantly. The corresponding R_a for 100 ppm acetaldehyde increased from 1.5×10^4 to 2.5×10^5 Ohm (pristine ZnO NSs to PdO@ZnO p–n heterojunction NSs), as shown in Fig. 7(b). Since the response is measured as R_a/R_g, the higher R_a for PdO@ZnO p–n heterojunction NSs results in an increased response, as compared to the pristine ZnO NSs sensor. Fig. 8(b) shows that the R_a value of the

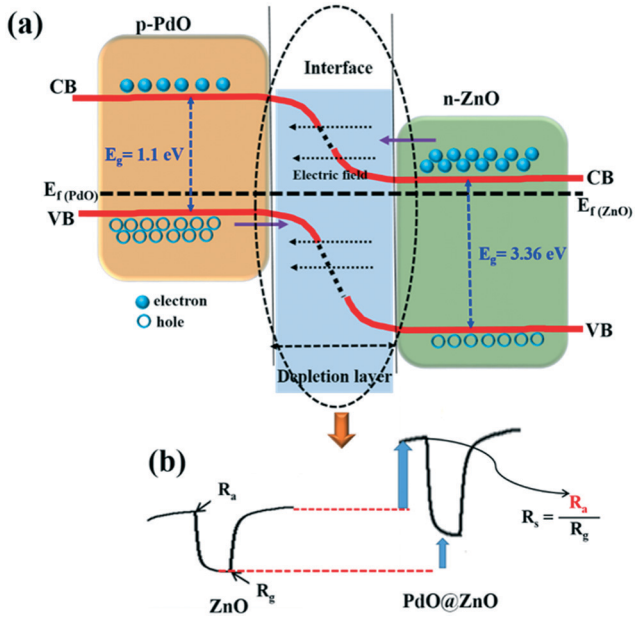

Fig. 8 (a) Schematic of the energy band diagram of PdO@ZnO p–n heterojunction NSs, and (b) response signals of the pristine ZnO NSs and PdO@ZnO p–n heterojunction NSs sensors showing the changes of R_a.

PdO@ZnO p–n heterojunction NSs is much higher than the R_a value of ZnO, which is due to the formation of the wider depletion layer between ZnO and PdO NPs. Once the acetaldehyde gas is introduced, these chemisorbed oxygen species will react with acetaldehyde gas molecules and release the trapped electrons back to the conduction bands of ZnO and PdO, resulting in the decreased resistance of the PdO@ZnO p–n heterojunction NSs sensor, which is denoted as R_g. Even the value of R_g in the PdO@ZnO p–n heterojunction NSs is higher than the R_g value of ZnO. Hence, the electronic sensitization effect is responsible for enhancing the R_a value.

In addition to the electronic sensitization effect, PdO NPs play an important role in the chemical sensitization effect, which is also known as the catalytic spillover effect. In the case of the PdO@ZnO p–n heterojunction NSs sensor, similar to ZnO NSs, a depletion layer is formed due to the trapping of electrons by chemisorbed oxygen species (in this study it was O^-). However, in this case a wider depletion layer forms between PdO and ZnO NPs in the PdO@ZnO p–n heterojunction NSs sensor, as shown in Fig. 9(a). The reason behind this is the chemical sensitization effect of PdO NPs in the system, because the PdO NPs act as a catalyst, which facilitates the dissociation of oxygen molecules into O atoms:[46–48]

$$O_{2(gas)} \leftrightarrow 2O_{(ads)} \quad (3)$$

Some of these O atoms can diffuse and then spill over onto ZnO surfaces, where they can trap electrons from the conduction band of ZnO to form adsorbed O^- ions on the sensor surface:[49,50]

$$O_{(ads)} + e^-(\text{from ZnO}) \leftrightarrow O_{(ads)}^- \quad (4)$$

This phenomenon results in the increase of the number of chemisorbed oxygen species on the PdO@ZnO p–n heterojunction NSs, as compared to that on the pristine ZnO NSs. In this situation, a greater number of electrons will be extracted from ZnO, which eventually increases the depletion layers between the ZnO and PdO NPs, resulting a wider depletion layer and band bending at the interface as shown in the schematic in Fig. 9(b). This results in high potential barriers (qV) (Fig. 9(b)) between the intergranular ZnO NPs and PdO NPs, which hinder the conduction of electrons, thus increasing the resistance of the sensor. After the acetaldehyde gas is exposed, the chemisorbed oxygen ions (O^-) will react with acetaldehyde gas molecules and release the trapped electrons back to the conduction bands of ZnO and PdO NPs. This results in the lowering of the potential barrier height (Fig. 9(b)) and decrease of the resistance of the PdO@ZnO p–n heterojunction NSs. Hence, the chemical sensitization effect accelerates the sensing reaction with improved sensing performance.

Moreover, the PdO NPs not only increase the sites for oxygen molecule and target gas adsorption, but also lower the activation energy that is required for the gas-sensing reaction.[51] Therefore, the response of the PdO@ZnO p–n heterojunction NSs is much higher. Furthermore, it was reported that PdO can be reduced to Pd, with electrons being donated

Table 1 Comparison of the sensing properties of the PdO@ZnO p–n heterojunction NSs sensor with previously reported sensors

Materials	Target gas/concentration (ppm)	Operating temperature (°C)	Response (R_a/R_g) or $[(R_a - R_g)/R_g]^a$	Ref.
Au@SnO_2 CSNSs	Acetaldehyde/200	400	0.85[a]	3
Au@ZnO CSNSs	Acetaldehyde/100	300	52	24
Al doped ZnO NSs	Acetaldehyde/10	500	2250[a]	37
ZnO tiny nanoplates	Acetaldehyde/100	RT	36	38
ZnO tetra pods	Acetaldehyde/50	400	47.5	39
ZnO nanorods	Acetaldehyde/250	300	2.5	40
0.1 Rh–SnO_2 NPs	Acetaldehyde/40	350	17.8	41
ZnO nanoflowers	Acetaldehyde/100	400	19	42
PdO@ZnO p–n heterojunction NSs	Acetaldehyde/100	350	76	The current work

[a] RT: room temperature.

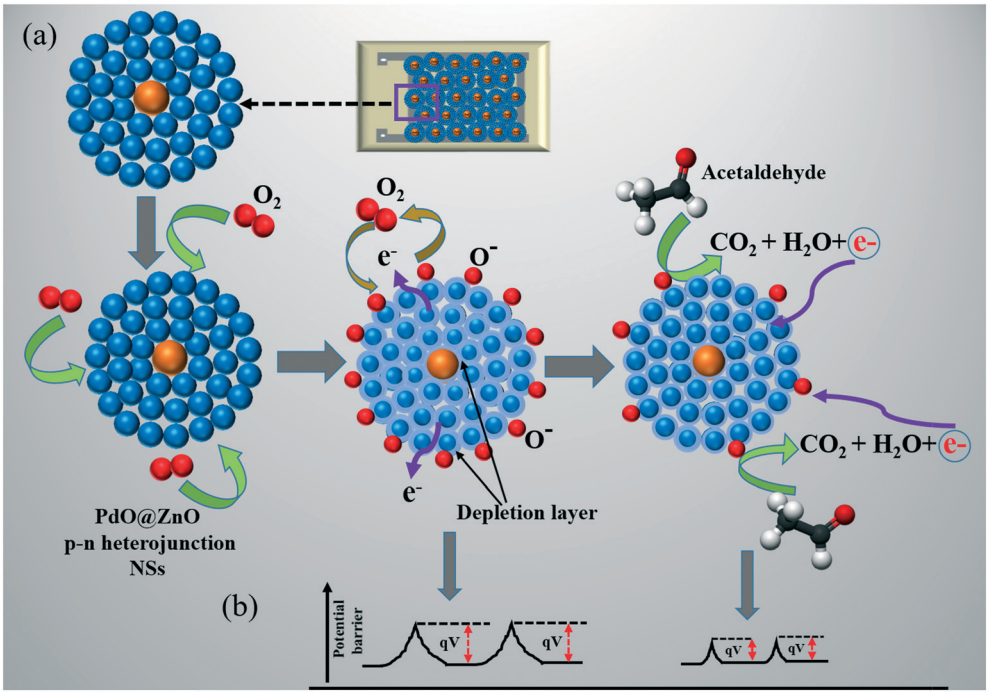

Fig. 9 (a) Schematic of the gas sensing mechanism for the PdO@ZnO heterojunction NSs-based sensor in air and acetaldehyde medium, with (b) potential barrier modulation.

back to the PdO@ZnO p–n heterojunction NSs sensor, when reducing gases like acetaldehyde are exposed to the sensor. This also results in the reduction of the width of the depletion layer, thereby inducing a large resistance change in the PdO@ZnO p–n heterojunction NSs sensor.[50] Also, the PdO@ZnO p–n heterojunction NSs-based sensor has a larger surface area, and therefore possesses more surface adsorption sites and more efficient gas diffusion (oxygen and target gases) as compared to the pristine ZnO NSs, which can facilitate the enhanced sensing performance.

5. Conclusions

In summary, we have developed a simple, low-temperature hydrothermal technique to synthesize Pd@ZnO CSNSs, and employed a simple high-temperature calcination strategy to construct PdO@ZnO p–n heterojunction NSs to investigate their gas-sensing performance. The XRD analysis of the prepared PdO@ZnO p–n heterojunction NSs revealed that the oxidation of Pd to PdO started from 300 °C, and further complete oxidation was confirmed at 500 °C after 2 h. The obtained flower-shaped, crystalline PdO@ZnO p–n heterojunction NSs were investigated as a gas sensor, and demonstrated the highest response (R_s = 76) and selectivity for 100 ppm acetaldehyde at 350 °C. The operating temperature of the PdO@ZnO p–n heterojunction NSs was also lower than the working temperature of the pristine ZnO NSs. The high sensing performance of the PdO@ZnO p–n heterojunction NSs sensor is mainly attributed to the synergistic effect of the p–n heterojunction, the catalytic dissociation of oxygen molecules by PdO NPs (chemical sensitization effect), and the high surface area of the PdO@ZnO p–n heterojunction NSs sensor. The present results confirm that the PdO@ZnO p–n heterojunction NSs-derived gas sensor is a promising sensing platform for high-response gas sensors. Notably, our proposed strategy would pave the way for the design of gas sensors based on novel core–shells, with various metals and MOs.

Conflicts of interest

There are no conflicts to declare.

Acknowledgements

This work was supported by (1) the BK21 plus program from the Ministry of Education and Human-Resource Development and (2) National Research Foundation of Korea (NRF) grants funded by the Korean government (MSIP) (BRL No. 2015042417 and 2016R1A2B4014090).

References

1 I. A. Avramescu, T. Noguer, M. Avramescu and J.-L. Marty, *Anal. Chim. Acta*, 2002, **458**, 203–213.
2 M. E. Ghica, R. Pauliukaite, N. Marchand, E. Devic and C. M. A. Brett, *Anal. Chim. Acta*, 2007, **591**, 80–86.
3 S. K. Tripathy, A. Mishra, S. K. Jha, R. Wahab and A. A. Al-Khedhairy, *Anal. Methods*, 2013, **5**, 1456–1462.
4 Y. Murashima, M. R. Karim, R. Furue, T. Matsui, H. Takehira, K. Wakata, K. Toda, R. Ohtani, M. Nakamura and S. Hayami, *Inorg. Chem. Front.*, 2016, **3**, 842–848.

5 K. Yamashita, M. Noguchi, A. Mizukoshi and Y. Yanagisawa, *Int. J. Environ. Res. Public Health*, 2010, **7**, 3489–3498.
6 R. K. Chava, H. Y. Cho, J. M. Yoon and Y. T. Yu, *J. Alloys Compd.*, 2019, **772**, 834–842.
7 C. Wang, L. Yin, L. Zhang, D. Xiang and R. Gao, *Sensors*, 2010, **10**, 2088–2106.
8 D. Wang, Z. Ma, S. Dai, J. Liu, Z. Nie, M. H. Engelhard, Q. Huo, C. Wang and R. Kou, *J. Phys. Chem. C*, 2008, **112**, 13499–13509.
9 A. Kolmakov, D. O. Klenov, Y. Lilach, S. Stemmer and M. Moskovits, *Nano Lett.*, 2005, **5**, 667–673.
10 H. Kim, C. Jin, S. Park, S. Kim and C. Lee, *Sens. Actuators, B*, 2012, **16**, 594–599.
11 X. Liu, X. Tian, X. Jiang, L. Jiang, P. Hou, S. Zhang, X. Sun, H. Yang, R. Cao and X. Xu, *Sens. Actuators, B*, 2018, 270304–270311.
12 X. Xue, L. Xing, Y. Chen, S. Shi, Y. Wang and T. Wang, *J. Phys. Chem. C*, 2008, **112**, 12157–12160.
13 J. H. Kim, J. H. Lee, A. Mirzaei, H. W. Kim and S. Sub Kim, *Sens. Actuators, B*, 2017, **248**, 500–511.
14 C. W. Na, H.-S. Woo, I.-D. Kim and J.-H. Lee, *Chem. Commun.*, 2011, **475**, 148–5150.
15 M. Reddeppa, B. G. Park, M. D. Kim, K. R. Peta, N. D. Chinh, D. Kim, S. G. Kim and G. Murali, *Sens. Actuators, B*, 2018, **264**, 353–362.
16 N. D. Chinh, N. D. Quang, H. Lee, T. T. Hien, N. M. Hieu, D. Kim, C. Kim and D. Kim, *Sci. Rep.*, 2016, **6**, 35066, (1–11).
17 H. S. Woo, C. W. Na and J. H. Lee, *Sensors*, 2016, **16**, 1531, (1–23).
18 L. Wang, J. Deng, Z. Lou and T. Zhang, *J. Mater. Chem. A*, 2014, **2**, 10022–10028.
19 W. J. Park, K. J. Choi, M. H. Kim, B. H. Koo, J. L. Lee and J. M. Baik, *ACS Appl. Mater. Interfaces*, 2013, **5**, 6802–6807.
20 J. H. Lee, J. H. Kim and S. S. Kim, *Appl. Surf. Sci.*, 2018, **448**, 489–497.
21 H. Tian, H. Fan, G. Dong, L. Ma and J. Ma, *RSC Adv.*, 2016, **6**, 109091–109098.
22 P. Rai, S. M. Majhi, Y. T. Yu and J. H. Lee, *RSC Adv.*, 2015, **5**, 76229–76248.
23 Y. T. Yu and P. Dutta, *Sens. Actuators, B*, 2011, **157**, 444–449.
24 S. M. Majhi, P. Rai and Y.-T. Yu, *ACS Appl. Mater. Interfaces*, 2015, **7**, 9462–9468.
25 F.-C. Chung, Z. Zhu, P. Y. Luo, R.-J. Wu and W. Li, *Sens. Actuators, B*, 2014, **199**, 314–319.
26 X. Li, X. Zhou, H. Guo, C. Wang, J. Liu, P. Sun, F. Liu and G. Lu, *ACS Appl. Mater. Interfaces*, 2014, **6**, 18661–18667.
27 F. Gu, H. Chen, D. Han and Z. Wang, *RSC Adv.*, 2016, **6**, 29727–29733.
28 X. W. Liu, F. Y. Wang, F. Zhen and J. R. Huang, *RSC Adv.*, 2012, **2**, 7647–7651.
29 Y. Gong, X. Wu, J. Chen, W. Li, N. Han, D. Zhang and Y. Chen, *New J. Chem.*, 2019, **43**, 2220–2230.
30 D. Acharya, K. Y. Huang, P. P. Chattopadhyay, M. S. Ho, H. J. Fecht and P. Bhattacharyya, *Analyst*, 2016, **141**, 2977–2989.
31 W. T. Koo, J. S. Jang, S. J. Choi, H. J. Cho and I. D. Kim, *ACS Appl. Mater. Interfaces*, 2017, **9**, 18069–18077.
32 Y. Yang, S. Han, G. Zhou, L. Zhang, X. Li, C. Zou and S. Huang, *Nanoscale*, 2013, **5**, 11808–11819.
33 S. M. Majhi, G. K. Naik, H. J. Lee, H. G. Song, C. R. Lee, I. H. Lee and Y. T. Yu, *Sens. Actuators, B*, 2018, **268**, 223–231.
34 K. S. W. Sing, D. H. Everett, R. A. W. Haul, L. Moscou, R. A. Pierotti, J. Rouquerol and T. Siemieniewka, *Pure Appl. Chem*, 1985, **57**, 603–619.
35 J. F. Chang, H. H. Kuo, I. C. Leu and M. H. Hon, *Sens. Actuators, B*, 2002, **84**, 258–264.
36 S. Zhang, W. Jiang, Y. Li, X. Yang, P. Sun, F. Liu, X. Yan, Y. Gao, X. Liang, J. Ma and G. Lu, *Sens. Actuators, B*, 2019, **291**, 266–274.
37 R. Yoo, D. Li, H. J. Rim, S. Cho, H. S. Lee and W. Y. Lee, *Sens. Actuators, B*, 2018, **266**, 883–888.
38 G. K. Mani and J. B. B. Rayappan, *RSC Adv.*, 2014, **4**, 64075–64084.
39 D. Calestani, R. Mosca, M. Zanichelli, M. Villani and A. Zappettini, *J. Mater. Chem.*, 2011, **21**, 15532–15536.
40 P. Rai, H. M. Song, Y. S. Kim, M. K. Song, P. R. Oh, J. M. Yoon and Y. T. Yu, *Mater. Lett.*, 2018, **68**, 90–93.
41 Y. Shimizu, K. Yamaguchi, K. Fukunga, Y. Takao, T. Hyodo and M. Egashira, *J. Electrochem. Soc.*, 1999, **146**, 1222–1226.
42 P. Rai and Y. T. Yu, *Sens. Actuators, B*, 2012, **173**, 58–65.
43 J. Zhang, Z. Qin, D. Zheng and C. Xie, *Phys. Chem. Chem. Phys.*, 2017, **19**, 6313–6329.
44 A. Mirzaei, S. S. Kim and H. W. Kim, *J. Hazard. Mater.*, 2018, **357**, 314–331.
45 X. Chen, Y. Shen, P. Zhou, S. Zhao, X. Zhong, T. Li, C. Han, D. Wei and D. Meng, *Sens. Actuators, B*, 2019, **280**, 151–161.
46 M. L. Hitchman, *J. Electroanal. Chem. Interfacial Electrochem.*, 1977, **85**, 135.
47 N. Matsuyama, S. Okazaki, H. Nakagawa, H. Sone and K. Fukuda, *Thin Solid Films*, 2009, **517**, 4650–4653.
48 R. Ahmed, S. M. Majhi, X. Zhang, T. M. Swager and K. N. Salama, *Adv. Colloid Interface Sci.*, 2019, **270**, 1–27.
49 N. Barsan and U. Weimar, *J. Electroceram.*, 2001, **7**, 143–167.
50 M. Zhao, J. X. Huang and C. W. Ong, *Sens. Actuators, B*, 2014, **191**, 711–718.
51 S.-J. Choi, S.-J. Kim, W.-T. Koo, H.-J. Cho and I.-D. Kim, *Chem. Commun.*, 2015, **51**, 2609–2612.

